Appendix to "Bedforms in a turbulent stream."

By A. Fourrière, P. Claudin& B. Andreotti

Journal of Fluid Mechanics, vol. 649 (2010), pp. 287–328

In this supplementary part, we first develop several aspects of the hydrodynamical description of a turbulent flow over a wavy bottom. In particular, we investigate the robustness of the results presented in the main paper with respect to (i) the order of the turbulent closure, (ii) the Reynolds stress anisotropy and (iii) the moving of the bottom boundary. None of these factors has a significant influence on the basal shear stress shift. We also study the effect of the mechanisms controlling the hydrodynamical roughness z_0, and especially investigate the case where the thickness of the surface layer h_0 is comparable to that of the inner layer ℓ. We furthermore present a friction force model, in which Navier-Stokes equations for a perfect flow are closed with a crude additional turbulent friction term as an approximation of the stress derivatives, and for which analytical expressions of the linear solution of the flow can be derived. In particular, the resonance condition as well as the behaviour of the basal stress for $kH \to 0$ can be found and interpreted. Finally, some technical considerations for the computation of the streamlines are detailed.

1. A second order turbulent closure

A first order closure assumes that the turbulent energy adapts instantaneously to the mean strain tensor. To take into account the lag between the stress and the strain tensors, one needs to formulate a second order turbulent closure.

1.1. *Relaxation equation*

The dynamical equations governing the second-order moments τ_{ik} can be derived rigorously. Under the assumption of turbulence isotropy at the dissipative scale, it can be written under the form:

$$D_t\tau_{ik} = \partial_t\tau_{ik} + u_j\partial_j\tau_{ik} = -\tau_{kj}\partial_j u_i - \tau_{ij}\partial_j u_k - \partial_j\phi_{ik} - \pi_{ik} - \frac{2}{3}\delta_{ik}\varepsilon. \tag{1.1}$$

ε is the dissipation rate; $\phi_{ik} = \overline{u'_i u'_j u'_k}$ is the spatial flux of turbulent energy induced by fluctuations; the pressure term $\pi_{ik} = \overline{u'_k\partial_i p'} + \overline{u'_i\partial_k p'}$ conserves energy and is usually responsible for the isotropisation of fluctuations.

We wish to get a stress tensor that relaxes towards its steady state expression

$$\tau_{ij} = \kappa^2 L^2|\dot\gamma|\left(\frac{1}{3}\chi^2|\dot\gamma|\,\delta_{ij} - \dot\gamma_{ij}\right), \tag{1.2}$$

see part 1. For dimensional reasons, we write the relaxation rate under the form $|\dot\gamma|/\beta$, where β is a phenomenological constant, and keep the mixing length L fixed by the geometrical distance to the wall. The second moment equation then takes the form of a first order relaxation equation:

$$D_t\tau_{ik} = \partial_t\tau_{ik} + u_j\partial_j\tau_{ik} = \frac{|\dot\gamma|}{\beta}\left[\kappa^2 L^2\left(\delta_{ij}\frac{1}{3}\chi^2|\dot\gamma|^2 - |\dot\gamma|\dot\gamma_{ij}\right) - \tau_{ij}\right]. \tag{1.3}$$

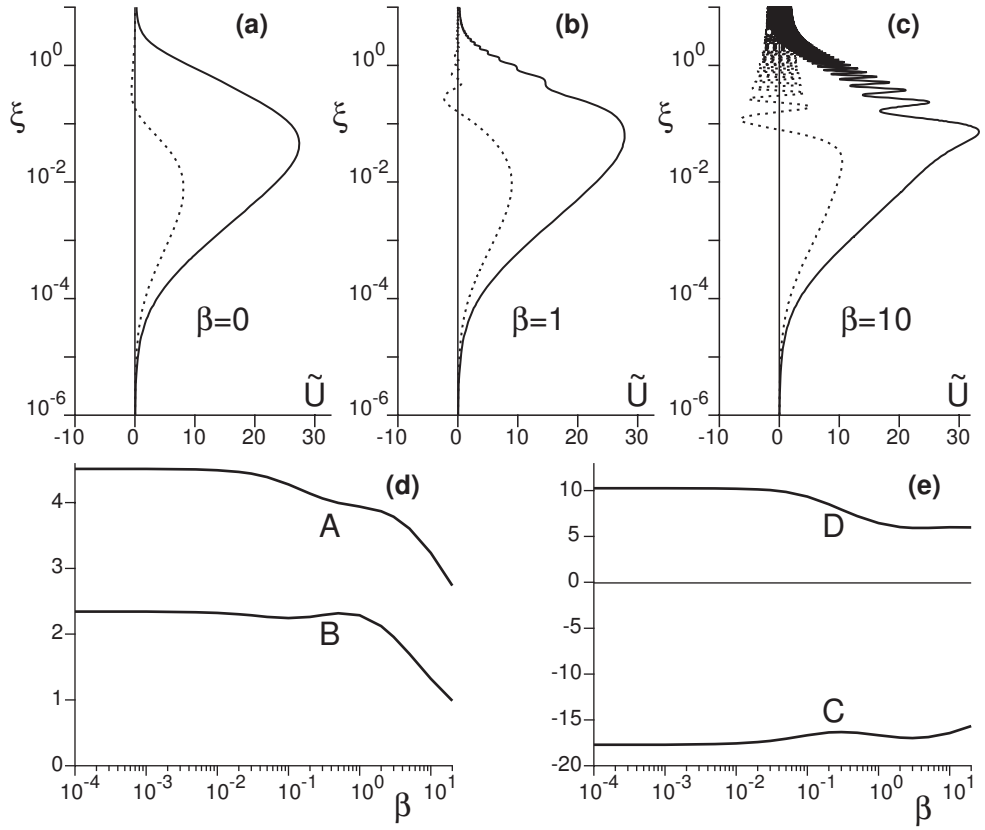

FIGURE 1. Effect of the parameter β,which is a non dimensional parameter encoding the time lag between a change in the strain rate and that of the Reynolds stress. (a-c) Vertical profiles of the horizontal component of the velocity $\tilde{U} = U + \mathcal{U}'$ for $\eta_0 = 10^{-4}$ for (a) $\beta = 0$, (b) $\beta = 1$ and (c) $\beta = 10$ respectively. One can see that the profiles develop oscillations as β increases, but that the behaviour close to the bottom (in log scale) remains the same. In panels (d) and (e), we plot the rescaled basal stress We note $\tilde{S}_t(0) = A + iB$ and $\tilde{S}_n(0) = C + iD$ *vs* β (still for $\eta_0 = 10^{-4}$). They are weakly affected, meaning again that the behaviour close to the bottom is almost unchanged.

Setting $\beta = 0$, one recovers the stationary solutions (1.2). A finite value of β introduces a lag between a change of the flow velocity field and the point/time at which the Reynolds stress readapts to this change.

1.2. *Equations for 2D steady flows*

For 2D steady situations, the stress relaxation equations are the following:

$$u_x\partial_x\tau_{xz} + u_z\partial_z\tau_{xz} = \frac{|\dot{\gamma}|}{\beta}\left[-\kappa^2 L^2|\dot{\gamma}|\dot{\gamma}_{xz} - \tau_{xz}\right], \tag{1.4}$$

$$u_x\partial_x\tau_{xx} + u_z\partial_z\tau_{xx} = \frac{|\dot{\gamma}|}{\beta}\left[-\kappa^2 L^2|\dot{\gamma}|\dot{\gamma}_{xx} + \frac{1}{3}\kappa^2\chi^2 L^2|\dot{\gamma}|^2 - \tau_{xx}\right], \tag{1.5}$$

$$u_x\partial_x\tau_{zz} + u_z\partial_z\tau_{zz} = \frac{|\dot{\gamma}|}{\beta}\left[-\kappa^2 L^2|\dot{\gamma}|\dot{\gamma}_{zz} + \frac{1}{3}\kappa^2\chi^2 L^2|\dot{\gamma}|^2 - \tau_{zz}\right]. \tag{1.6}$$

At linear order, they simplify into:

$$(\mathcal{U}' + i\beta\mathcal{U})S_t = 2(U' + iW) - 2\kappa^2(\eta + \eta_0)\mathcal{U}'^3, \tag{1.7}$$

$$(\mathcal{U}' + i\beta\mathcal{U})S_{xx} = -2iU + \frac{2}{3}\chi^2(U' + iW) - \frac{2}{3}\chi^2\kappa\mathcal{U}'^2, \tag{1.8}$$

$$(\mathcal{U}' + i\beta\mathcal{U})S_{zz} = -2W' + \frac{2}{3}\chi^2(U' + iW) - \frac{2}{3}\chi^2\kappa\mathcal{U}'^2. \tag{1.9}$$

Taking the difference of equations (1.8) and (1.9), one can compute

$$S_{xx} - S_{zz} = \frac{-4iU}{\mathcal{U}' + i\beta\mathcal{U}} \tag{1.10}$$

to obtain four closed equations:

$$U' = -iW + \frac{\mathcal{U}' + i\beta\mathcal{U}}{2}S_t + \kappa\mathcal{U}'^2, \tag{1.11}$$

$$W' = -iU, \tag{1.12}$$

$$S_t' = \left(i\mathcal{U} + \frac{4}{\mathcal{U}' + i\beta\mathcal{U}}\right)U + \mathcal{U}'W + iS_n, \tag{1.13}$$

$$S_n' = -i\mathcal{U}W + iS_t. \tag{1.14}$$

As before, they can be written in the usual compact matrix form

$$\frac{d}{d\eta}\vec{X} = \mathcal{P}\vec{X} + \vec{S}, \tag{1.15}$$

where $\vec{X} = (U, W, S_t, S_n)$, and now with

$$\mathcal{P} = \begin{pmatrix} 0 & -i & \frac{\mathcal{U}' + i\beta\mathcal{U}}{2} & 0 \\ -i & 0 & 0 & 0 \\ \left(i\mathcal{U} + \frac{4}{\mathcal{U}' + i\beta\mathcal{U}}\right) & \mathcal{U}' & 0 & i \\ 0 & -\mathcal{U}i & i & 0 \end{pmatrix}. \tag{1.16}$$

In figure 1, we show the effect of this new parameter. As expected for inertial effects in a relaxation process, finite values of β generate oscillations in the vertical profiles of the velocities and stresses. The example of the horizontal velocity is displayed in the panels (a), (b) and (c). The amplitude and the frequency of these oscillations increase with β. Interestingly, these oscillations do not affect much the behaviour of the modes close to the bottom. As a consequence, the basal shear stress $\tilde{S}_t(0) = A + iB$ and the basal normal stress $\tilde{S}_n(0) = C + iD$ are weakly affected by β, see panels (d) and (e). Interestingly, both A and B decrease as β increases and their ratio remains roughly constant. β has thus a negligible effect on the emergence of bedform.

2. Reynolds stress anisotropy

It is an experimental fact that, in a turbulent boundary layer close to a rough wall, the Reynolds stress tensor is *not* isotropic: τ_{xx} is significantly larger than the other components (Raupach et al. 1991, Shafi & Antonia 1995). Besides, anisotropy seems less pronounced for a larger bottom roughness (Krogstad & Antonia 1994, Keirsbulck et al. 2002), an issue which is however still matter of debate (Krogstad et al. 2005).

To account for this Reynolds stress anisotropy, it is easy to generalise the Prandtl-like

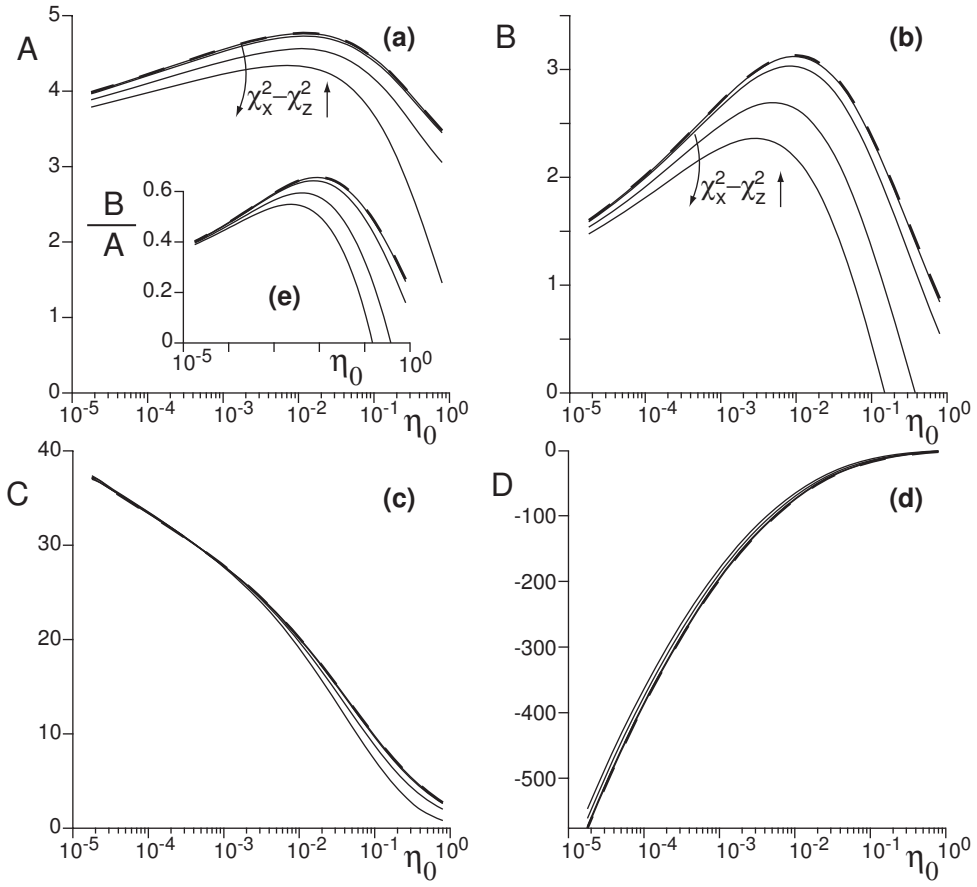

FIGURE 2. Effect of the normal stress anisotropy. (a-d) Coefficients A, B, C and D as a function of η_0 for different values of $\chi_x^2 - \chi_z^2$ (0.1, 1, 5 and 10). The dashed lines correspond to the isotropic case. Inset (e): ratio B/A. Arrows indicate increasing normal stress anisotropy.

first order turbulent closure (1.2) with the following expression:

$$\tau_{ij} = \kappa^2 L^2 |\dot{\gamma}| \left(\frac{1}{3} \chi_i^2 |\dot{\gamma}| \, \delta_{ij} - \dot{\gamma}_{ij} \right), \tag{2.1}$$

where the value of χ_x now differs from that of χ_z. Following the above-cited literature, we expect χ_x^2/χ_z^2 to be around 1.3–1.5. At the linear order, the velocity, pressure and stress fields read:

$$u_x = u_* \left[\mathcal{U} + k\zeta e^{ikx} U \right], \tag{2.2}$$

$$u_z = u_* k\zeta e^{ikx} W, \tag{2.3}$$

$$\tau_{xz} = \tau_{zx} = -u_*^2 \left[1 + k\zeta e^{ikx} S_t \right], \tag{2.4}$$

$$p + \tau_{zz} = p_0 + u_*^2 \left[\frac{1}{3} \chi_z^2 + k\zeta e^{ikx} S_n \right], \tag{2.5}$$

$$\tau_{zz} = u_*^2 \left[\frac{1}{3} \chi_z^2 + k\zeta e^{ikx} S_{zz} \right], \tag{2.6}$$

$$\tau_{xx} = u_*^2 \left[\frac{1}{3} \chi_x^2 + k\zeta e^{ikx} S_{xx} \right], \tag{2.7}$$

and the stress equations can be simplified into

$$\mathcal{U}'S_t = 2(U' + iW) - 2\kappa^2(\eta + \eta_0)\mathcal{U}'^3, \tag{2.8}$$

$$\mathcal{U}'S_{xx} = -2iU + \frac{2}{3}\chi_x^2(U' + iW) - \frac{2}{3}\chi_x^2\kappa\mathcal{U}'^2, \tag{2.9}$$

$$\mathcal{U}'S_{zz} = -2W' + \frac{2}{3}\chi_z^2(U' + iW) - \frac{2}{3}\chi_z^2\kappa\mathcal{U}'^2. \tag{2.10}$$

The normal stress difference is this time:

$$S_{xx} - S_{zz} = \frac{-4iU}{\mathcal{U}'} + \frac{2}{3}\frac{\chi_x^2 - \chi_z^2}{\mathcal{U}'}(U' + iW - \kappa\mathcal{U}'^2)\,, \tag{2.11}$$

so that on gets the following four closed equations:

$$U' = -iW + \frac{1}{2}\mathcal{U}'S_t + \kappa\mathcal{U}'^2, \tag{2.12}$$

$$W' = -iU, \tag{2.13}$$

$$S_t' = \left(i\mathcal{U} + \frac{4}{\mathcal{U}'}\right)U + \mathcal{U}'W + \frac{i}{3}(\chi_x^2 - \chi_z^2)S_t + iS_n, \tag{2.14}$$

$$S_n' = -i\mathcal{U}W + iS_t. \tag{2.15}$$

As before, they can be written in the usual compact matrix form, now with

$$\mathcal{P} = \begin{pmatrix} 0 & -i & \frac{1}{2}\mathcal{U}' & 0 \\ -i & 0 & 0 & 0 \\ (i\mathcal{U} + \frac{4}{\mathcal{U}'}) & \mathcal{U}' & \frac{i}{3}(\chi_x^2 - \chi_z^2) & i \\ 0 & -\mathcal{U}i & i & 0 \end{pmatrix}. \tag{2.16}$$

The relevant anisotropic parameter entering the equations is $\chi_x^2 - \chi_z^2$, for which a realistic value is on the order of unity. As evidenced in figure 2, the corresponding values of the functions A, B, C and D are not much affected by this anisotropy in the relevant range of η_0. This is particularly true for the coefficients C and D, as well as for the ratio B/A as soon as $\eta_0 < 10^{-2}$. The normal stress anisotropy has thus a negligible influence on ripple and dune formation.

3. A moving bottom

In order to investigate the effect of a moving bottom on the stress coefficients, we consider a bottom profile of wavevector k, which is function of both position x and time t:

$$Z(x,t) = \zeta\, e^{\sigma t}\, e^{i(kx - \omega t)}\,. \tag{3.1}$$

In this expression, σ represents the growth rate of the profile, and ω/k its phase velocity. As discussed in Colombini & Stocchino 2005, this investigation is important as we wish to use the present hydrodynamical study in the context of the formation and development of bedforms, which do have a (small) growth rate and a (small) velocity. Following expression (3.1), we modify those for the functions U, W, S_t and S_n by inserting the extra-factor $e^{(\sigma - i\omega)t}$, which now read:

$$u_x = u_* \left[\mathcal{U} + k\zeta\, e^{\sigma t}\, e^{i(kx - \omega t)}\, U\right], \tag{3.2}$$

$$\tag{3.3}$$

$$u_z = u_*\, k\zeta\, e^{\sigma t}\, e^{i(kx - \omega t)}\, W\,, \tag{3.4}$$

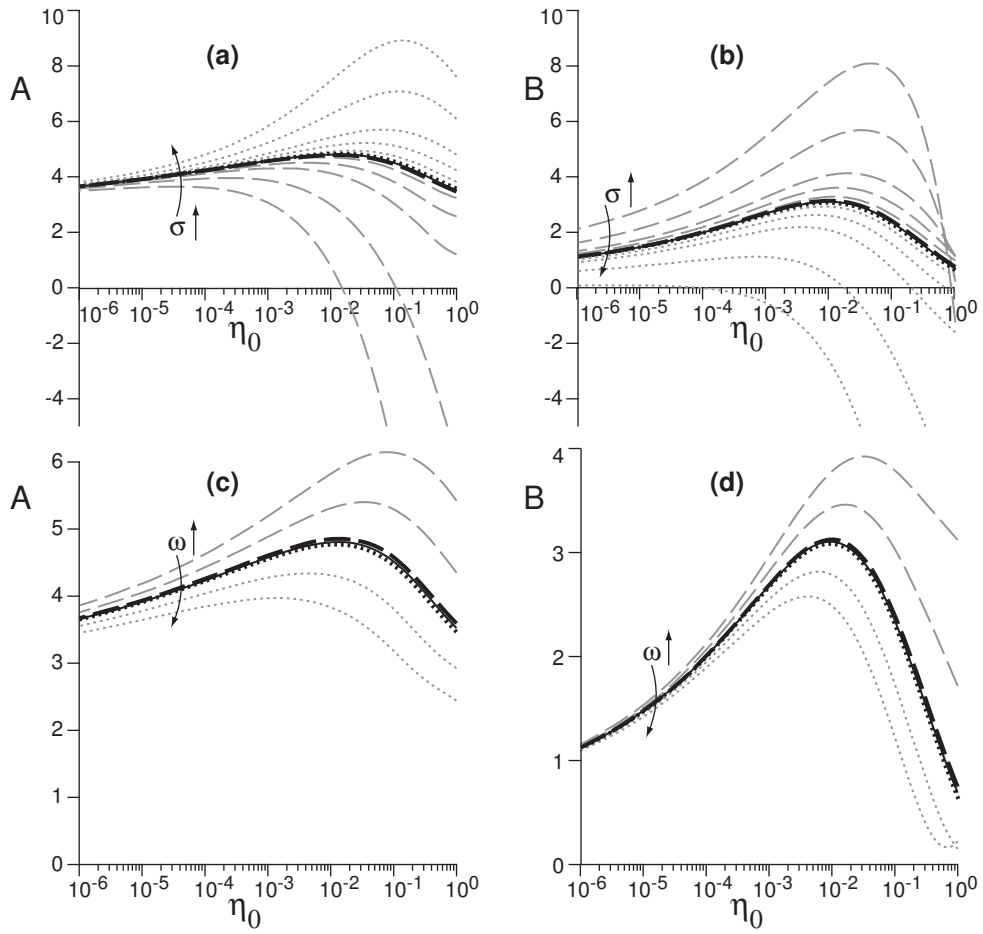

FIGURE 3. Effect of the motion of the bottom. Stress coefficients A and B as a function of η_0 for different values of the bottom growth rate σ (panels (a) and (b)), and different values of the bottom pulsation ω (panels (c) and (d)). Arrows indicate increasing values of σ and ω. In panels (a) and (b), grey dotted lines correspond to $\frac{\sigma}{ku_*} = 10$, 5, 2, 1 and 0.5, the black dotted line being for $\frac{\sigma}{ku_*} = 0.1$. The black dashed line corresponds to $\frac{\sigma}{ku_*} = -0.1$, the grey dashed lines being for $\frac{\sigma}{ku_*} = -0.5$, -1, -2, -5 and -10. In panels (c) and (d) grey dotted lines correspond to $\frac{\omega}{ku_*} = 2$ and 1, the black dotted line being for $\frac{\omega}{ku_*} = 0.1$. The black dashed line correspond to $\frac{\omega}{ku_*} = -0.1$, the grey dashed line being for $\frac{\omega}{ku_*} = -1$ and -2. For comparison, in all panels the solid lines correspond to the static case $\sigma = 0$, $\omega = 0$.

$$\tau_{xz} = \tau_{zx} = -\rho\, u_*^2 \left[1 + k\zeta\, e^{\sigma t}\, e^{i(kx-\omega t)}\, S_t \right] , \tag{3.5}$$

$$\tag{3.6}$$

$$p + \tau_{zz} = p_0 + \rho\, u_*^2 \left[\chi^2/3 + k\zeta\, e^{\sigma t}\, e^{i(kx-\omega t)}\, S_n \right] , \tag{3.7}$$

$$\tag{3.8}$$

$$\tau_{xx} = \rho\, u_*^2 \left[\chi^2/3 + k\zeta\, e^{\sigma t}\, e^{i(kx-\omega t)}\, S_{xx} \right] , \tag{3.9}$$

$$\tag{3.10}$$

$$\tau_{zz} = \rho\, u_*^2 \left[\chi^2/3 + k\zeta\, e^{\sigma t}\, e^{i(kx-\omega t)}\, S_{zz} \right] . \tag{3.11}$$

In this new case, the linearised Navier-Stokes equations of section 3 in part 1 must then be modified in the following manner:

$$S'_t = \left(\frac{\sigma}{ku_*} - i\frac{\omega}{ku_*} + i\mathcal{U} \right) U + \mathcal{U}'W + iS_n + iS_{xx} - iS_{zz} \,, \tag{3.12}$$

$$S'_n = -\left(\frac{\sigma}{ku_*} - i\frac{\omega}{ku_*} + i\mathcal{U} \right) W + iS_t \,. \tag{3.13}$$

The final linear equation is then the same, but now with the modified matrix

$$\mathcal{P} = \begin{pmatrix} 0 & -i & \frac{1}{2}\mathcal{U}' & 0 \\ -i & 0 & 0 & 0 \\ \frac{4}{\mathcal{U}'} + \frac{\sigma}{ku_*} + i\left(\mathcal{U} - \frac{\omega}{ku_*}\right) & \mathcal{U}' & 0 & i \\ 0 & -\frac{\sigma}{ku_*} - i\left(\mathcal{U} - \frac{\omega}{ku_*}\right) & i & 0 \end{pmatrix}. \tag{3.14}$$

With the surface layer model described in section 4.1 (Part 1), the non-slip boundary conditions on the bottom can be written as

$$U(0) = -\mathcal{U}'(0) \qquad \text{and} \qquad W(0) = \frac{\sigma}{ku_*} - i\frac{\omega}{ku_*} \,. \tag{3.15}$$

The result of the integration of this new system is shown in figure 3 for the shear coefficients A and B. One can see that departure from the static case $\sigma = 0$ and $\omega = 0$ is noticeable only for values of $\frac{\sigma}{ku_*}$ and $\frac{\omega}{ku_*}$ of order one. The effect of the wave propagation of the bedform can be understood by a simple argument. When the bedforms propagate upstream ($\omega < 0$) the relative flow velocity seen by the structure is larger so that it induces a larger shear stress modulation. As $A + iB$ is by definition the basal shear stress rescaled by u_*^2, both A and B get larger. Reciprocally, when the bedforms propagate downstream ($\omega > 0$), these coefficients are reduced. Consistently with this argument, the ratio B/A is only weakly affected by ω (not shown). The growth rate σ affects A and B in opposite ways and thus changes the phase shift between the shear stress and the topography. For $\sigma > 0$, A is increased while B is reduced. We have not been able to interpret this behaviour in a simple way.

It is also interesting to investigate how the resonance is affected by the fact that the bottom moves i.e. can grow or propagate. We display in figure 4 the amplitude of the free surface $|\delta|$ as a function of kH for different values of the growth rate σ and the pulsation ω. For positive growth rates σ, the Q-factor of the resonance gets smaller but the resonant wavenumber is not affected. A bottom propagating at the velocity ω/k moves the resonant peak along the kH-axis. For a positive propagation velocity ω/k the surface velocity with respect to the bottom and thus the effective Froude number get reduced. As a consequence, the resonant wavelength gets smaller – and kH larger. Conversely, the peak moves to smaller wavenumber for an upstream moving bottom.

For ripples in water flows the dimensionless numbers $\frac{\sigma}{ku_*}$ and $\frac{\omega}{ku_*}$ are respectively on the order of 10^{-3} and 10^{-2}. They would be even smaller for bedforms of larger wavelength. These values are too small to lead to noticeable effects. The bedform motion can thus be safely ignored in the hydrodynamical calculation and the effect of free surface interpreted in terms of surface standing waves.

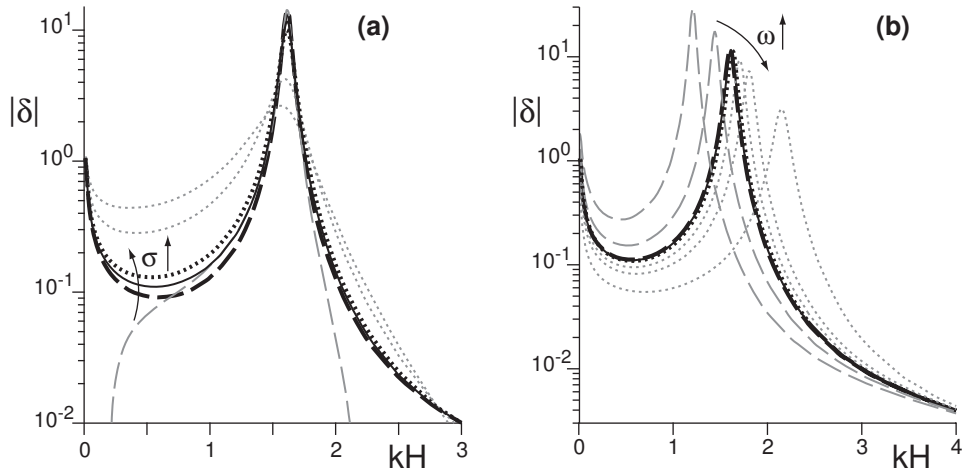

FIGURE 4. Amplitude of the free surface $|\delta|$ as a function of kH for different values of the growth rate σ (a) and the pulsation ω (b) of the bottom boundary. Arrows indicate increasing values of σ and ω. These graphs have been computed with $H/z_0 = 10^4$ and $\mathcal{F} = 0.8$. In panel (a), the grey dashed line is for $\frac{\sigma}{ku_*} = -1$, the back dashed line for -0.1, the black dotted line for 0.1 and the two grey dotted lines for 1 and 2. In panel (b), the two grey dashed lines is for $\frac{\omega}{ku_*} = -5$ and -2, the black dashed line for -0.1, the black dotted line for 0.1 and the three grey dotted lines for 1, 2 and 5. For comparison, in all panels the solid lines correspond to the fixed case $\sigma = 0$, $\omega = 0$.

4. Effect of the mechanisms controlling the hydrodynamical roughness

So far, the computation of the velocity and stress fields has been obtained without any specification of the physics at the scale of z_0, as the integration of equation (2.37) of the main paper is started in the inner layer rather than on the bottom. This is of course possible only if this layer is sufficiently thick, i.e. if ℓ (or λ) is much larger than the thickness of the surface layer h_0. We here discuss several ways to describe the flow inside the surface layer, and investigate the subsequent effect on the shape of the stress coefficients as functions of η_0. These coefficients should be independent of the physics at work in this surface layer when η_0 is small enough, but we expect larger differences for larger values of η_0.

We first present a convenient phenomenological model of geometrically induced roughness, which does not involve additional parameters. We then consider the case of a viscous surface layer. Inspired from the aeolian transport properties, we finally discuss the focus point assumption as a possible way to describe the situation in which the surface layer is governed by the presence of sediment transport.

4.1. *Geometrically induced roughness*

For an hydrodynamically rough bottom, the 'small scale' roughness elements are larger than the viscous sub-layer. They are submitted to a turbulent drag from the fluid and reciprocally, their presence slows down the flow. The exchanges of momentum in the surface layer are thus dominated by the turbulent fluctuations. Following Richards 1980 and others, a convenient phenomenological model is to define the mixing length involved in the turbulent closure as $L = z_0 + z - Z$. In this way, L is still essentially the geometrical distance to the bottom, except that it cannot be smaller than the roughness length. This choice reflects, in an intuitive manner, the physical picture one can infer from experiments

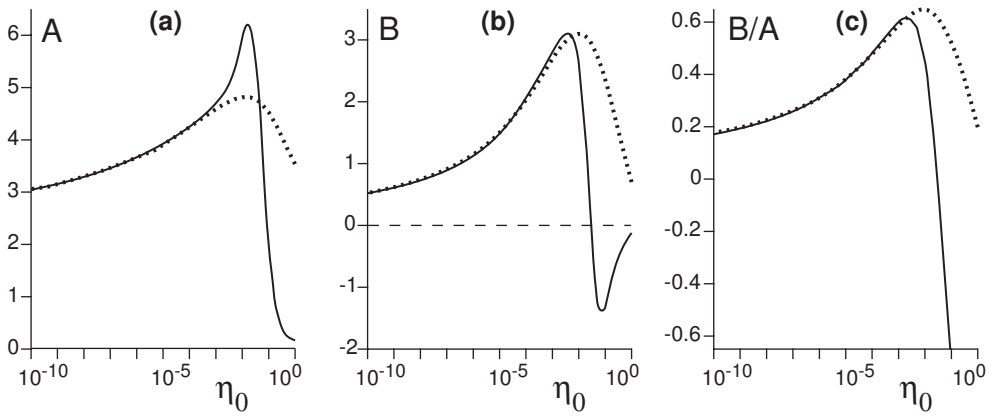

FIGURE 5. Shear stress coefficients A and B (dashed lines) computed with the phenomenological model of geometrically induced roughness (4.1). For comparison, the solid lines display the reference case shown in figure 4 of the main paper.

or simulations where square-shaped roughness elements are glued on a flat wall (see e.g. Perry et al. 1969).

With this expression for the mixing length, the integration of starting equations in the uniform and steady case gives

$$u_x = \frac{u_*}{\kappa} \ln\left(1 + \frac{z}{z_0}\right), \tag{4.1}$$

where the lower boundary condition $u_x = 0$ can now be taken in $z = 0$. This expression is well approximated by the pure logarithmic profile as soon as z is larger than, say, few z_0. In other words, for this model, $h_0 \sim z_0$.

The above description of the linear analysis, and in particular the expression of the matrix $\mathcal{P}$ and the vector $\mathcal{S}$ involved in equation (2.37) of the main paper, in the case of a wavy bottom is still valid, but now with the following expression for the function

$$\mathcal{U}(\eta) = \frac{1}{\kappa} \ln\left(1 + \frac{\eta}{\eta_0}\right). \tag{4.2}$$

The solution of this equation can again be written as a linear superposition $\vec{X} = \vec{X}_s + S_t(0)\vec{X}_t + S_n(0)\vec{X}_n$, where these three vectors are solutions of

$$\frac{d}{d\eta}\vec{X}_s = \mathcal{P}\vec{X}_s + \vec{S} \qquad \text{with} \qquad \vec{X}_s(0) = \begin{pmatrix} -\frac{1}{\kappa\eta_0} \\ 0 \\ 0 \\ 0 \end{pmatrix}, \tag{4.3}$$

$$\frac{d}{d\eta}\vec{X}_t = \mathcal{P}\vec{X}_t \qquad \text{with} \qquad \vec{X}_t(0) = \begin{pmatrix} 0 \\ 0 \\ 1 \\ 0 \end{pmatrix}, \tag{4.4}$$

$$\frac{d}{d\eta}\vec{X}_n = \mathcal{P}\vec{X}_n \qquad \text{with} \qquad \vec{X}_n(0) = \begin{pmatrix} 0 \\ 0 \\ 0 \\ 1 \end{pmatrix}. \tag{4.5}$$

This decomposition ensures the requirement that both components of the velocity vanish

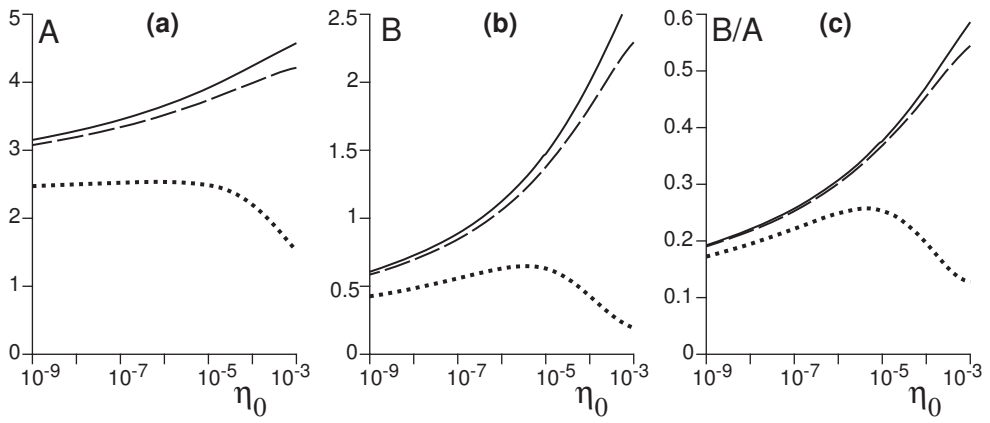

FIGURE 6. Shear stress coefficients A and B computed with a viscous surface layer. Dotted line: $\mathcal{R}_t = 125$; Dashed line: $\mathcal{R}_t = 1$. As in figure 5, the solid lines display the reference case shown in figure 4 of the main paper.

on the bottom, leading to $W(0) = 0$ and $U(0) = -\mathcal{U}'(0) = -1/(\kappa\eta_0)$. As in the previous section, the coefficients $S_t(0)$ and $S_n(0)$ are found by the upper boundary conditions.

The coefficients A and B resulting from this integration are displayed in figure 5. One can see that, for $\eta_0 < 10^{-3}$, they are not very much different from those obtained in the previous section. However, one can notice significant differences for $\eta_0 > 10^{-2}$. As the mixing length in the surface layer is larger in this case ($L \sim z_0$) than in the asymptotic case ($L \sim z - Z$), the turbulent 'diffusion' is more efficient. This results into a larger phase advance for the shear stress, see figure 5c. For practical purposes and for later use in the second part of this paper, a very good empirical fit of the coefficients A and B is obtained by expressing them as a function of and $R = \ln \frac{2\pi}{\eta_0}$:

$$A = 2 + \frac{a_1 + a_2 R + a_3 R^2 + a_4 R^3}{1 + a_5 R^2 + a_6 R^4} \quad \text{and} \quad B = \frac{b_1 + b_2 R + b_3 R^2 + b_4 R^3}{1 + b_5 R^2 + b_6 R^4} \tag{4.6}$$

with $\{a_1, a_2, a_3, a_4, a_5, a_6\} = \{1.0702, 0.093069, 0.10838, 0.024835, 0.041603, 0.0010625\}$, $\{b_1, b_2, b_3, b_4, b_5, b_6\} = \{0.036989, 0.15765, 0.11518, 0.0020249, 0.0028725, 0.00053483\}$.

4.2. *A viscous surface layer*

In hydraulically smooth situations, it is natural to expect that, very close to the bottom, the flow must be laminar and thus described by the equation

$$\tau = \nu \frac{du_x}{dz} = u_*^2, \tag{4.7}$$

whose solution is

$$u_x(z) = \frac{u_*^2}{\nu} z. \tag{4.8}$$

We thus neglect here the possibility of a phase shift across the viscous surface layer. The transition from viscous to turbulent regime is governed by the Reynolds number $\mathcal{R} = \frac{z\, u_x}{\nu}$ and occurs at a typical value $\mathcal{R}_t \simeq 125$. The surface layer thickness can then be easily computed as $h_0 = \frac{\nu}{u_*}\sqrt{\mathcal{R}_t}$. At $z = h_0$, both viscous and turbulent expressions for the velocity must coincide:

$$u_h \equiv u_* \sqrt{\mathcal{R}_t} = \frac{u_*}{\kappa} \ln \frac{h_0}{z_0}\,. \tag{4.9}$$

From this equality, we can deduce the hydrodynamical roughness seen from the inner layer, due to this viscous surface layer:

$$z_0 = \frac{\nu}{u_*}\sqrt{\mathcal{R}_t}\, e^{-\kappa\sqrt{\mathcal{R}_t}}. \tag{4.10}$$

In the case of a sand bed, the transition between the hydrodynamically smooth and rough regimes occurs when the viscosity induced roughness (Eq. 4.10) is of the order of the geometrically induced roughness ($z_0 \sim d/10$).

With the corresponding value for $\eta_0 = kz_0$, we solve equation (2.37) of the main paper in the usual manner, writing the solution in the form of the linear superposition as described above, except that the integration is started at the initial value $\eta = kh_0$, in which we impose that the velocity is parallel to the bed and equal to u_h. At linear order, this leads to

$$U(kh_0) = -\mathcal{U}'(kh_0), \tag{4.11}$$

$$W(kh_0) = iu_h/u_* = i\mathcal{U}(kh_0). \tag{4.12}$$

The resulting shear stress coefficients A and B are displayed in figure 6. As one can expect, in comparison to the reference case, they are smaller for larger values of $\mathcal{R}_t$, and all different curves collapse as $\eta_0 \to 0$. The viscous diffusion of momentum is less efficient than that induced by turbulent fluctuations. Moreover, in the Stokes regime, for Reynolds numbers much smaller than 1, the kinematic reversibility leads to a shear stress in phase with the topography. Consistently, it can be observed in figure 6c that the phase advance is reduced in the hydrodynamically smooth regime.

Experiments in the hydraulically smooth regime have been performed by Zilker et al. 1977, Zilker & Hanratty 1977, Abrams & Hanratty 1985, who measured the ionic mobility between two nearby electrodes. This current is assumed to be related, without any spatial or temporal lag, to the basal shear stress. The measured phase shift between the signal and the bottom topography could reach values as high as 80°. This would correspond to $B/A = \tan(80\pi/180) \simeq 5.67$. Within the present model, the phase shift remains much lower than the measured 80°. This unexpected high value has been interpreted as the signature of a lag of the laminar-turbulent transition with respect to the Reynolds number criterion $\mathcal{R} = \mathcal{R}_t$. Further experiments based on a different measure principle are needed to understand this discrepancy.

This viscous surface layer model is an effective way to take bedload transport into account. As a matter of fact, transported particles are not passive and exert a stress on the fluid. Close to the transport threshold, their influence on the flow is negligible. However, as their concentration increases, transport induces a negative feedback on the flow, which should be taken into consideration in the hydrodynamics description. The simplest model of multi-layer sheet flow would be a Newtonian fluid whose viscosity increases with the concentration of moving sediments. In this large shear velocity regime, one thus expects a decrease of the phase-lag responsible for the ripples instability and possibly, a restabilisation of the bed.

4.3. *The focus point assumption*

An alternative manner to take the feedback of the transport on the flow into account can be achieved in analogy with the aeolian case, which provides the archetype of such a situation. In this case, it has been shown that the moving grains slow down the flow in the transport layer, whose thickness h_0 is independent of the shear velocity u_*. Note that in the subaqueous case, the transport layer thickness is observed to gently increase with the shear stress (Abbott & Francis 1977, Fernandez Luque & van Beek 1976) close to

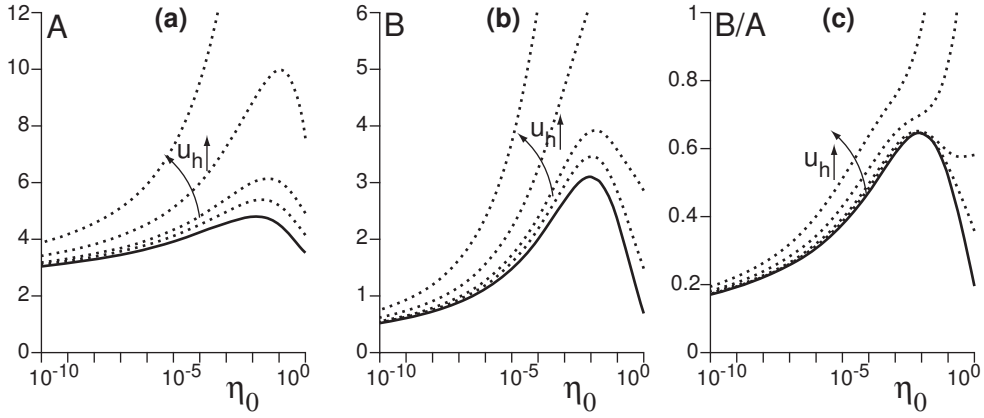

FIGURE 7. Shear stress coefficients A and B computed in the presence of a 'focus point' at height h_0, where the velocity is u_h, as a function of η_0. A and B are larger for larger values of u_h/u_* (1, 2, 5 and 10). However, the ratio B/A is less sensitive to this parameter, up to $\eta_0 \simeq 10^{-3}$. Again, the solid lines display the reference case of figure 4 (main paper).

the threshold, in the erosion limited regime. Above h_0, the effect of the particles on the flow is negligible and one recovers the undisturbed logarithmic velocity profile, but with a roughness larger than that without transport. Below h_0, the flow velocity is reduced and is independent of u_* (Ungar & Haff 1987, Andreotti 2004). As shown experimentally by Bagnold 1941, the velocity vertical profiles measured for different shear velocities thus cross at the 'focus point' $z = h_0$ and $u_x = u_h$. At this point we have

$$\frac{u_h}{u_*} = \frac{1}{\kappa} \ln \frac{h_0}{z_0}\,, \tag{4.13}$$

which means that the effective roughness in the logarithmic region, due to this transport layer, is

$$z_0 = h_0\, e^{-\kappa u_h/u_*} \tag{4.14}$$

To determine the flow field in such a situation, the crucial point is to compare h_0 with the thickness of the inner layer ℓ, i.e. the size of the constant stress plateau (see figure 2 of the main paper). If h_0 is larger than ℓ, it means that one cannot reduce the transport issue to a relationship between the sediment flux and the basal shear stress only. In that case, the whole vertical velocity profile, which depends on the entire bottom elevation, is involved. Conversely, for $h_0 < \ell$, one can account for transport by modifying the bottom boundary conditions as follows. Following what we have done in the previous sub-section, we can impose that the fluid velocity at $z = Z + h_0$ is parallel to the bed and equal to u_h. At the linear order, we then get:

$$U(kh_0) = -\mathcal{U}'(kh_0) \tag{4.15}$$

$$W(kh_0) = iu_h/u_* = i\mathcal{U}(kh_0). \tag{4.16}$$

The result of this choice is shown for the stress coefficients in figure 7 for various values of u_h/u_*. A and B are larger for increasing focus velocities, or equivalently larger focus altitude. As in the viscous surface layer case, all curves collapse for $\eta_0 \to 0$ because ℓ gets larger in this limit (see equation (2.48) of the main paper). Interestingly, as far as bedforms are concerned, the ratio B/A is much less sensitive to variations of u_h/u_*, at least in the region $\eta_0 < 10^{-3}$.

Finally, it should be noted that the focus point model only applies to the momentum

limited transport regime. Close to the transport threshold, in the erosion limited regime, the feedback of the particle transport on the flow is negligible and the transport should not to be taken into account in the hydrodynamical calculation.

4.4. *Concluding remarks*

For these three dynamical mechanisms controlling the hydrodynamical roughness z_0, we have seen that the asymptotic regime is recovered when the surface layer thickness h_0 is smaller than the inner layer thickness ℓ. As ℓ is much smaller than the wavelength λ (for standard bedforms, $\ell/\lambda = \mathcal{O}(10^{-3})$), this constitutes a rather restrictive condition. Whenever h_0 is larger than ℓ, specific hydrodynamic models should be derived to determine the relations between stresses and topography.

The phase shift between the basal shear stress and the topography originates from the interplay between inertia and shear stress. The different models of surface layer correspond to different ways of mixing momentum in the direction normal to the wall. Although the argument is general, one sees that the precise value of the phase shift is rather sensitive to the physical origin of the momentum fluxes. In particular, viscous diffusion leads to a much smaller phase advance than turbulent mixing.

5. A friction force closure

Several of the free surface effects can be recovered within a simple friction force model, for which analytical expressions of the linear solution of the flow can be derived. In particular, the resonance condition as well as the behaviour of the basal stress coefficients A, B, C and D for $kH \to 0$ can be found and interpreted.

5.1. *Reference state*

We start from the Navier-Stokes equations for a perfect flow, with a crude additional turbulent friction term as an approximation of the stress derivatives:

$$\partial_x u_x + \partial_z u_z = 0, \tag{5.1}$$

$$u_x \partial_x u_x + u_z \partial_z u_x = -\partial_x p + g \sin\theta - \Omega \frac{u_x}{H} u_x, \tag{5.2}$$

$$u_x \partial_x u_z + u_z \partial_z u_z = -\partial_z p - g \cos\theta - \Omega \frac{2u_x}{H} u_z, \tag{5.3}$$

Physically, the force applied to a fluid particle is directly related to the relative velocity with respect to the ground. At an angle θ, the following plug flow is an homogeneous solution of the above equations:

$$u_x = \overline{u} = \sqrt{\frac{gH \sin\theta}{\Omega}}\,, \tag{5.4}$$

$$u_z = 0\,, \tag{5.5}$$

$$p = g \cos\theta (H - z). \tag{5.6}$$

In order to estimate the value of the friction coefficient, one can make use of the fact that typical turbulent velocity vertical profiles are logarithmic. However, as the logarithm varies slowly when z is much larger than z_0, we write $\overline{u} \sim \frac{1}{H}\int_0^H dz\, u_x(z) \sim \frac{u_*}{\kappa}\left(\ln\frac{H}{z_0} - 1\right)$. Identifying the shear stress on the bottom as $u_*^2 = gH\sin\theta$, we finally get with the relation (5.4)

$$\Omega \sim \left(\frac{\kappa}{\ln\frac{H}{z_0} - 1}\right)^2. \tag{5.7}$$

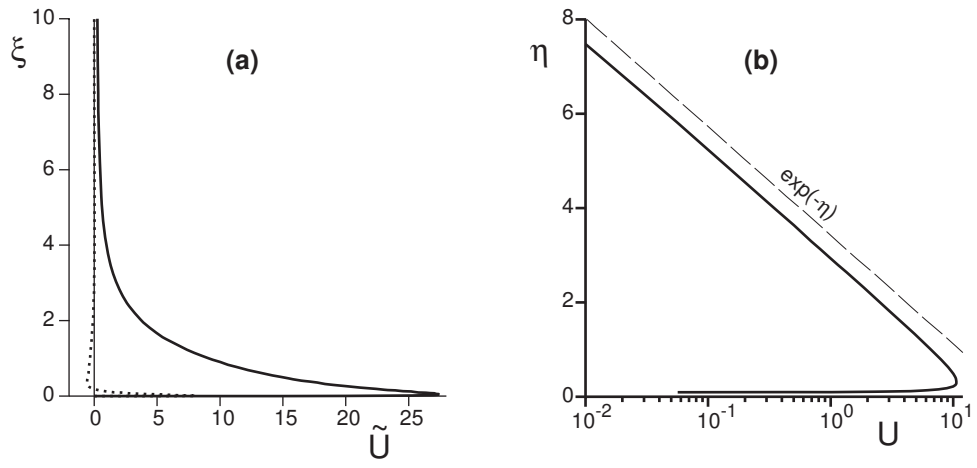

FIGURE 8. Vertical profiles of the first order correction to the horizontal velocity computed with the full model for $\eta_0 = 10^{-4}$. (a) Lin-lin plot in the shifted representation. (b) Lin-Log plot in the non-shifted representation. The solid lines correspond to the real part and the dotted line to the imaginary one. The velocity disturbance decreases exponentially over one wavelength (dashed line). In this outer region, the Reynolds stress can be neglected.

For H/z_0 in the range 10^3-10^4, we get a typical value for Ω on the order of few 10^{-3}. We now normalize quantities by $\overline{u}$ and H and get a single non-dimensional (Froude) number:

$$\mathcal{F} = \frac{\overline{u}}{\sqrt{gH\cos\theta}}\,. \tag{5.8}$$

5.2. *Disturbance*

The starting equations can be linearised around the above reference state. Looking a the flow over a corrugated bottom $Z(x) = \zeta e^{ikx}$, it is easy to show that the solution is of the following form

$$u_x = \overline{u} + \overline{u}k\zeta e^{ikx}\left[-a_+e^{kz} + a_-e^{-kz}\right], \tag{5.9}$$

$$u_z = \overline{u}ik\zeta e^{ikx}\left[a_+e^{kz} + a_-e^{-kz}\right], \tag{5.10}$$

$$p = g\cos\theta(H-z) + \overline{u}^2(kH - i2\Omega)\frac{\zeta e^{ikx}}{H}\left[a_+e^{kz} - a_-e^{-kz}\right], \tag{5.11}$$

where a_+ and a_- must be determined by the boundary conditions. This exponential form is characteristic of potential flows. In figure 8, we display for comparison the velocity vertical profiles computed with the full model. The exponential behaviour is found in the outer region where the Reynolds stress can be neglected.

5.3. *Boundary conditions*

We require that the velocity normal to the bottom vanish. Following the notations of the main part of the paper, we define Δ such that the free surface is at the altitude $H+\Delta$. It is a material line where the pressure vanishes. The three boundary conditions are then:

$$u_z(z=0) = i\overline{u}k\zeta e^{ikx}, \tag{5.12}$$

$$u_z(z=H) = i\overline{u}\delta k\zeta e^{ikx}, \tag{5.13}$$

$$p(z=H) = \frac{\overline{u}^2}{H\mathcal{F}^2}\,\delta\zeta e^{ikx}, \tag{5.14}$$

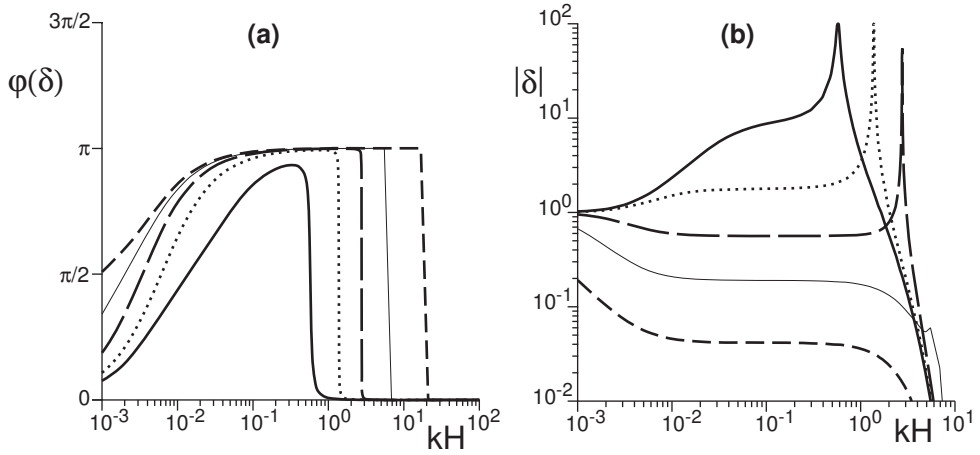

FIGURE 9. The phase (a) and amplitude (b) of the rescaled free surface deformation $\delta = \Delta/\zeta$ as a function of kH for $\mathcal{F} \to 0$ (dotted dashed line), $\mathcal{F} = 0.2$ (dashed line), $\mathcal{F} = 0.4$ (thin solid line), $\mathcal{F} = 0.6$ (long dashed line), $\mathcal{F} = 0.8$ (dotted line) and $\mathcal{F} = 1$ (solid line), and $H/z_0 = 10^3$. Crossing the resonance, the phase shifts from 0 to π. These plots are very similar to those displayed in figure 16 of part 1, where the very same quantities are computed with the full model.

where, as before, δ is defined as $\Delta(x) = \delta\zeta e^{ikx}$. The constants a_+ and a_-, as well as δ are thus solutions of

$$a_+ + a_- = 1\,, \tag{5.15}$$

$$a_+ e^{kH} + a_- e^{-kH} = \delta\,, \tag{5.16}$$

$$a_+ e^{kH} - a_- e^{-kH} = \frac{\delta}{(kH - i2\Omega)\mathcal{F}^2}\,, \tag{5.17}$$

from which we get:

$$a_+ = \frac{1}{2}\left[1 - \frac{(kH - i2\Omega)\tanh kH - \frac{1}{\mathcal{F}^2}}{(kH - i2\Omega) - \frac{1}{\mathcal{F}^2}\tanh kH}\right], \tag{5.18}$$

$$a_- = \frac{1}{2}\left[1 + \frac{(kH - i2\Omega)\tanh kH - \frac{1}{\mathcal{F}^2}}{(kH - i2\Omega) - \frac{1}{\mathcal{F}^2}\tanh kH}\right]. \tag{5.19}$$

From these analytical expressions, one can compute the phase and amplitude of the rescaled free surface deformation δ, see figure 9. They reproduce very well the results of the full model (see Part 1). As one can see from the above expressions, the amplitude of the surface deformation is maximum when $kH - \frac{1}{\mathcal{F}^2}\tanh kH = 0$. This situation corresponds to the resonance of the surface waves with the bottom undulations. In figure 10, we display variations of δ with $\mathcal{F}$ and kH, computed with the full model.

5.4. *Basal shear stress and pressure*

The shear stress is not part of the variables of this model, but we can consistently define it as $\tau = -\Omega u_x^2$. Looking at the shear stress τ_b and normal stress p_b on the bottom, in accordance with the notations of the paper, we introduce the coefficients A, B, C and D as

$$\tau_b = -\Omega\overline{u}^2\left[1 + (A + iB)k\zeta e^{ikx}\right], \tag{5.20}$$

$$p_b = gH\cos\theta + \Omega\overline{u}^2(C + iD)k\zeta e^{ikx}, \tag{5.21}$$

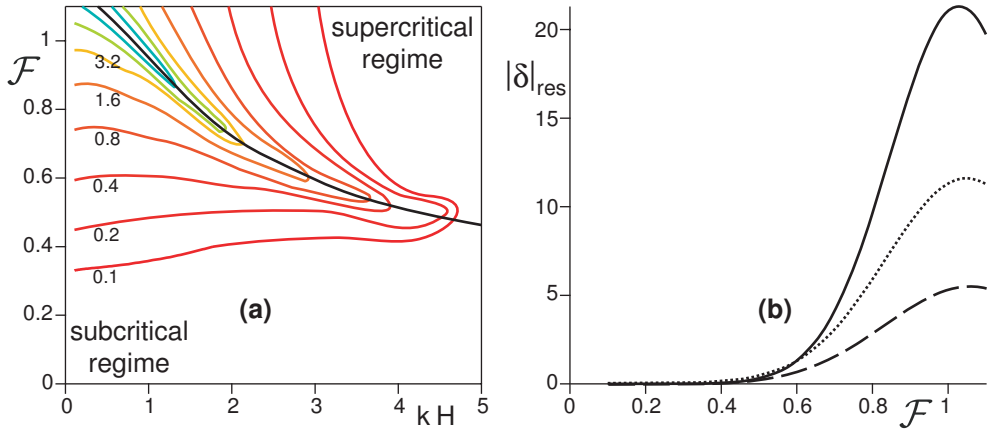

FIGURE 10. Amplitude $|\delta|$ of the distortion of the free surface related to that of the bedform, computed with the full model. (a) Isocontours of $|\delta|$ in the plane $\mathcal{F}$ vs kH. (b) Distortion $|\delta|$ computed along the resonance curve (black solid line in panel (a) for $H/z_0 = 10^2$ (dashed line), $H/z_0 = 10^3$ (dotted line) and $H/z_0 = 10^4$ (solid line) as a function of the Froude number $\mathcal{F}$. The amplitude in the resonant conditions is maximum at $\mathcal{F} \simeq 1$.

which gives

$$A = 2\,\frac{\left[(kH)^2 + 4\Omega^2 + \frac{1}{\mathcal{F}^4}\right]\tanh kH - \frac{1}{\mathcal{F}^2}\,kH[\tanh^2 kH + 1]}{\left(kH - \frac{1}{\mathcal{F}^2}\tanh kH\right)^2 + 4\Omega^2}\,, \tag{5.22}$$

$$B = \frac{2\Omega}{\mathcal{F}^2}\,\frac{[\tanh^2 kH - 1]}{\left(kH - \frac{1}{\mathcal{F}^2}\tanh kH\right)^2 + 4\Omega^2}\,, \tag{5.23}$$

$$C = \frac{1}{2\Omega}\left(-A - \frac{2\Omega B}{kH}\right), \tag{5.24}$$

$$D = \frac{1}{2\Omega}\left(-B + \frac{2\Omega A}{kH}\right). \tag{5.25}$$

It is worth noting that the friction force model predicts negative values of B for any kH. This means that there is always a phase delay of the shear stress with respect to the bottom, which is a clear disagreement with the full solution. In order to fix this flaw, one would need to empirically introduce an imaginary part to Ω. Finally, this discrepancy shows that a precise description of the phase between the basal friction and the relief is a subtle and difficult issue that fully justifies the use of a more rigorous but heavier formalism.

6. Stream function

To compute the streamlines, we introduce the so-called stream function $\Psi(x, z)$, defined by $\partial\Psi/\partial x = -u_z$ and $\partial\Psi/\partial z = u_x$. This function is such that $\vec{u}\cdot\vec{\nabla}\Psi = 0$, so that the iso-contours $\Psi = \text{Cst}$ precisely show the streamlines. Using the continuity equation, it is easy to show that a solution is $\Psi = \int d\check{z}\, u_x$. This integral is computed between $\check{z} = Z$ (the bottom) and $\check{z} = z$. We note $\xi = \eta - kZ$ the rescaled distance to the bottom. Restricting to the linear order, with the relation $U_1 = iW_1'$, we end up with

$$\Psi = \frac{u_*}{k}\left\{(\xi + \eta_0)\mathcal{U}(\xi) - \frac{1}{\kappa}\xi + k\zeta e^{ikx}\left[iW_1(\xi) + \mathcal{U}(\xi)\right]\right\}, \tag{6.1}$$

where the function $\mathcal{U}$ is given by the expression (4.2).

In the situation with a free surface, one can use the following representation for the field f:

$$f = \bar{f}(\xi) + k\zeta e^{ikx}\tilde{f}_1(\xi), \quad \text{with} \quad \xi = \eta_H \frac{z - Z}{H + \Delta - Z}\,. \tag{6.2}$$

This curvilinear variable ξ vanishes on the bottom $z = Z$, and $\xi = \eta_H$ at the surface $z = H + \Delta$. The new function $\tilde{f}_1$ is related to those of the non-shifted representation $\bar{f}$ and f_1 as:

$$\tilde{f}_1(\xi) = f_1(\xi) + \left(1 + (\delta - 1)\frac{\xi}{\eta_H}\right)\bar{f}'(\xi). \tag{6.3}$$

For $f = u_x$, we have $\bar{f} = \mathcal{U}$ and $f_1 = U_1 = iW_1'$. Consequently, the new stream function is

$$\Psi_{FS} = \frac{u_*}{k}\left\{(\xi + \eta_0)\mathcal{U}(\xi) - \frac{1}{\kappa}\xi + k\zeta e^{ikx}\left[iW(\xi) + \mathcal{U}(\xi) + (\delta - 1)\frac{\xi\mathcal{U}(\xi)}{\eta_H}\right]\right\}. \tag{6.4}$$

One can check that the free surface is indeed a streamline itself, as one of the top boundary conditions is $W_1(\eta_H) = i\mathcal{U}(\eta_H)\delta$.

REFERENCES

Abbott, J.E. & Francis, J.R.D. 1977 Saltation and suspension trajectories of solid grains in a water stream. *Phil. Trans. R. Soc. London* **284**, 225-254.

Abrams J. & Hanratty, T.J. 1985 Relaxation effects observed for turbulent flow over a wavy surface. *J. Fluid Mech.* **151**, 443-455.

Andreotti B. 2004 A two species model of aeolian sand transport. *J. Fluid Mech.* **510**, 47-50.

Bagnold, R.A. 1941 The physics of blown sand and desert dunes. Methuen, London.

Colombini, M. & Stocchino, A. 2005 Coupling or decoupling bed and flow dynamics: Fast and slow sediment waves at high Froude numbers. *Phys. Fluids 17*, 036602.

Fernandez Luque, R. & van Beek, R. 1976 Erosion and transport of bed-load sediment. J. Hydraul. Res. 14, 127-144.

Keirsbulck, L., Labraga, L., Mazouz, A. & Tournier, C. 2002 Influence of surface roughness on anisotropy in a turbulent boundary layer flow. *Exp. Fluids* **33**, 497-499.

Krogstad, P.-Å., Andersson, H.I., Bakken, O.M. & Ashrafian, A. 2005 An experimental and numerical study of channel flow with rough walls. *J. Fluid Mech.* **530**, 327-252.

Krogstad, P.-Å. & Antonia, R.A. 1994 Structure of turbulent boundary layers on smooth and rough walls. *J. Fluid Mech.* **277**, 1-21.

Perry, A.E., Schofield, W.H. & Joubert, P.N. 1969 Rough wall turbulent boundary layers. *J. Fluid Mech.* **37**, 383-413.

Raupach, M. R., Antonia, R. A. & Rajagopalan, S. 1991 Rough-wall turbulent boundary layers. *Appl. Mech. Rev.* **44**, 1-25.

Richards, K.J. 1980 The formation of ripples and dunes on an erodible bed. *J. Fluid Mech.* **99**, 597-618.

Shafi, H. S. & Antonia, R. A. 1995 Anisotropy of the Reynolds stresses in a turbulent boundary layer on a rough wall. *Exp. Fluids* **18**, 213-215.

Ungar, J.E. & Haff, P.K. 1987 Steady-state saltation in air, Sedimentology **34**, 289-300.

Zilker, D.P., Cook, G.W. & Hanratty, T.J. 1977 Influence of the amplitude of a solid wavy wall on a turbulent flow. Part 1. Non-separated flows. *J. Fluid Mech.* **82**, 29-51.

Zilker, D.P. & Hanratty, T.J. 1979 Influence of the amplitude of a solid wavy wall on a turbulent flow. Part 2. Separated flows. *J. Fluid Mech.* **90**, 257-271.